metals

MDPI

Article

Structure of Eutectic Al-Si Alloy Subjected to Compression Plasma Flow Impact

Natallia Bibik [1], Alexander Metel [2], Nikolai Cherenda [1], Catherine Sotova [2], Valiantsin Astashynski [3], Anton Kuzmitski [3], Yury Melnik [2] and Alexey Vereschaka [4,*]

[1] Department of Solid State Physics and Nanotechnology, Belarusian State University, 220030 Minsk, Belarus; bibiknv@bsu.by (N.B.); cherenda@bsu.by (N.C.)
[2] Department of High-Efficiency Machining Technologies, Moscow State University of Technology "STANKIN", Moscow 127055, Russia; a.metel@stankin.ru (A.M.); e.sotova@stankin.ru (C.S.); yu.melnik@stankin.ru (Y.M.)
[3] Department of Plasma Physics and Plasma Technologies, A.V. Lykov Heat and Mass Transfer Institute of the National Academy of sciences of Belarus, 220072 Minsk, Belarus; ast@hmti.ac.by (V.A.); antey@hmti.ac.by (A.K.)
[4] Institute of Design and Technological Informatics of the Russian Academy of Sciences (IDTI RAS), Moscow 127055, Russia
* Correspondence: dr.a.veres@yandex.ru

Abstract: The structure and phase composition of a eutectic silumin surface layer modified by compression plasma flow impact were investigated in this work. Plasma flows were generated by a magnetoplasma compressor of a compact geometry in a nitrogen atmosphere. The energy density absorbed by the surface layer was varied in the range of 10–35 J/cm^2. X-ray diffraction analysis, scanning electron microscopy, transmission electron microscopy and X-ray microanalysis were used as investigation techniques. It was found that the plasma impact led to the formation of a molten layer with a thickness of up to 50 μm. The layer thickness increased with the growth of the absorbed energy density. Dissolution of the intermetallic compounds and primary silicon crystals occurred as a result. The modified surface layer contained grains of a supersaturated solid silicon solution in aluminum. Grains with sizes of 100–500 nm were separated by interlayers of hypereutectic silumin containing nanocrystalline silicon precipitates. The doping elements of the alloy were concentrated mainly in these interlayers. The plasma impact resulted in a 1.5-fold microhardness increase.

Keywords: eutectic Al-Si alloy; compression plasma flows; phase composition; microstructure; microhardness

Citation: Bibik, N.; Metel, A.; Cherenda, N.; Sotova, C.; Astashynski, V.; Kuzmitski, A.; Melnik, Y.; Vereschaka, A. Structure of Eutectic Al-Si Alloy Subjected to Compression Plasma Flow Impact. *Metals* **2024**, *14*, 1415. https://doi.org/10.3390/met14121415

Academic Editor: Thomas Niendorf

Received: 8 November 2024
Revised: 2 December 2024
Accepted: 5 December 2024
Published: 10 December 2024

1. Introduction

Aluminum alloys are widely used in various fields of industry: automobile and aircraft manufacturing, space, energy, construction, the food industry, etc. An intensive annual growth of these alloys' production volume has been observed [1–4]. The share of cast-aluminum alloys used in these industries is about 20%, and 90% of it is Al-Si alloys (which are called silumins) [5]. This group of alloys possesses low densities, good castabilities, corrosion and heat resistance, electrical and heat conductivity, high specific strengths, resistance to dynamic loads and low costs [5–14]. It has been considered that Al-Si alloys have the best strength properties among other light alloys [7]. A powerful stimulus for the use of Al-Si alloys in industry was the discovery of the phenomenon of aluminum–silicon eutectic and primary silicon crystal modification with surface-active substances: in particular, sodium, phosphorus, strontium and a number of other substances [11,15,16].

All industrial Al-Si alloys are doped with additional elements that form eutectics with Al-Si in order to increase their strength properties and susceptibility to heat treatment. The main alloying elements of Al-Si alloys are magnesium and copper and, less often, nickel, manganese, zinc, chromium, etc. [5,17–20]. Piston silumins are one of the most complexly doped groups of Al-Si alloys, which are used to manufacture pistons for internal combustion engines. These alloys work in extreme operating conditions associated with high temperatures and pressures and high cyclic loads. Further increases in silumins' strength properties by alloying are limited by the solubility limit of the alloying elements in Al, which does not exceed 0.1% for most of the alloying elements [5].

Al-Si alloy use in industry is often limited because of the presence of large-scale crystalline structures such as primary silicon crystals and Al-Si-Fe phases in these alloys [7,8,10,21]. These are the reasons for the low values of the mechanical properties of these alloys [8–10,21]. So, the mechanical properties of Al-Si depend not only on the chemical composition but are strongly influenced by the uniformity and dispersity of the alloy microstructure [10]. A number of conventional techniques are used nowadays to refine the microstructures of Al-Si alloys and to increase their mechanical properties: heat treatments, modification of chemical composition and the use of electromagnetic treatments [8,10,22]. The use of high-energy particle beams, such as ion, laser and electron beams, for the modification of alloy surface layer properties is also of interest [7,23–35]. Such an approach allows increased microhardness [7,23,26,30,31], wear resistance [26,30] and corrosion resistance [31] and diminished friction coefficients [26].

There are a number of ways to generate plasma flows and high-energy particle beams, particularly in ion–plasma deposition systems [36–38]. Treatment by high-energy particle beams in a melting mode is a prospective method of aluminum–silicon alloy modification [26,30]. The melting of surface layers followed by crystallization in conditions of high cooling speed leads to the strong dispersion of near-surface microstructures, the dissolution of primary silicon crystals and intermetallic compounds and the formation of metastable phases, thus resulting in mechanical property improvement [26,28–35]. In particular, it was reported that the treatment of an (Al-10 %Si-2 %Cu)-alloy by an intensive pulsed electron beam with a beam energy density of 10–50 J/cm^2 led to the dissolution of silicon, the formation of a sub-micro-sized crystal structure of high-speed cellular crystallization forms and the saturation of an Al-based crystal lattice with alloying and impurity elements [7]. The microhardness value after the treatment was 1.6 times higher than that of the untreated material as a result [7]. The sizes of aluminum solid-solution grains depend on the chemical composition of the alloy and the treatment regimes. In [29], it was found that high-intensity electron beam treatment led to the formation of aluminum-based solid solution grains with sizes of 100–450 nm in an (Al-10.65 %Si-2.11 %Cu)-alloy and grains with sizes of 40–100 nm for an (Al-5.39 %Si-1.33 %Cu)-alloy. In addition, the formation of silicon nanocrystallites with sizes of 5–10 nm on the grain boundaries was revealed [29].

Compression plasma flows (CPFs) generated by quasi-stationary plasma accelerators can be also effectively used for the modification of Al-Si alloys. These plasma flows possess relatively high discharge times (hundreds of microseconds) and low divergence [39–41]. Previously conducted studies [41–44] have shown that CPF treatment of materials allows the formation of thick surface layers (a few tens of micrometers) with a dispersed structure. CPF impact leads to material surface layer melting, liquid-phase mixing of the structural components of the alloy due to the action of hydrodynamic instabilities arising at the plasma-melt boundary and subsequent crystallization under conditions of ultra-fast cooling (up to 10^7 K/s). CPF treatment causes significant changes in material structural-phase states and, hence, the mechanical properties of the surface layer [41–44].

By now, a relatively large volume of data have been accumulated on the modification of the structure and properties of silumin surface layers under the actions of ion and electron beams in melting mode. However, the physical processes occurring under the action of compression plasma flows on the surfaces of materials can differ in nature and intensity

from the processes observed under ion and electron impact, even at close values of energy absorbed by the surface layer. At the same time, investigations describing the influence of direct action of compression plasma flows on the properties and structure of eutectic silumins at the micro- and nanoscale levels have not been previously carried out. Thus, the study of the industrial eutectic Al-Si alloy structure after compression plasma flows impact was the aim of this work.

2. Materials and Methods

The investigation focused on samples composed of 11.0–13.0% Si, 0.8–1.5% Cu, 0.8–1.3% Mg, 0.2% Zn, 0.2% Mn, 0.2% Ti, 0.8–1.3% Ni, and the with the remaining percentage being aluminum. These samples were treated using compression plasma flows generated by a compact magnetoplasma compressor (Laboratory installation, A.V. Lykov Heat and Mass Transfer Institute of the National Academy of sciences of Belarus, Minsk, Belarus) [43,44]. The treatment occurred in residual gas mode, where a pre-evacuated vacuum chamber was filled with nitrogen at a pressure of 400 Pa. The processing involved three plasma pulses, with the energy density absorbed by the surface layer per pulse ranging from 10 to 35 J/cm^2, as measured by calorimetric assessments [42].

The phase composition of the samples was analyzed using X-ray diffraction (XRD) on a Rigaku Ultima IV diffractometer (Rigaku Corporation, Tokyo, Japan) in Bragg–Brentano focusing mode with CuKα radiation. Phase analysis was performed by comparing experimentally determined values of interplanar spacing and relative intensities against standard data from the PDXL2 Rigaku Data Analysis Software (Version 2.8.4.0 Rigaku Corporation, Tokyo, Japan).

The lattice parameter a of the aluminum was determined from the following relation:

$$\frac{1}{d^2} = \frac{H^2+K^2+L^2}{a^2}, \quad (1)$$

where d is the interplanar spacing (nm), and H, K and L are Miller indices.

The relative error of the interplanar distance was determined from the following relation:

$$\left|\frac{\Delta d}{d}\right| = ctg\theta\Delta\theta, \quad (2)$$

where θ is the Bragg diffraction angle, and $\Delta\theta$ is the step size of the diffraction angle change.

The microstructure of the surface layer was examined using a Carl Zeiss LEO1455VP scanning electron microscope (SEM) (Carl Zeiss AG, Oberkochen, Germany) operating at an accelerating voltage of 20 kV, equipped with an Oxford MaxN energy-dispersive microanalyzer (Oxford Instruments, Abingdon, UK) , as well as a JEM-2100 transmission electron microscope (TEM) (JEOL, Ltd., Tokyo, Japan) at an accelerating voltage of 200 kV. Samples were cut perpendicular to the treated surface with an ABRASIMET cutting machine (Struers, Balleron, Denmark) to allow for cross-sectional analysis using the SEM. They were then ground and polished using the Struers mold method (Struers, Denmark, Balleron) on a TegraPol setup (Struers, Denmark, Balleron), employing materials recommended by Struers. The fabrication and standard thinning procedures for the lamella used in TEM studies were performed using gallium-focused ion beam (FIB) Strata FIB 205 System (FEI Company, Hillsboro, Oregon, USA) at 30 kV. The elemental composition was analyzed using an INCA Energy EDX TEM system (OXFORD Instruments, Abingdon, UK). Measurements of the microhardness of the surface layers were conducted on a Wilson Instruments MVD 402 microhardness tester (Wilson Instruments, Shanghai, China) using the Vickers method. In this technique, a diamond Vickers indenter, shaped like a tetrahedral pyramid with a vertex angle of α=136°, was pressed into the sample surface under load. The indenter was maintained under load for 10 s during each measurement. After removing the load, the lengths of the two diagonals of the indent were measured, and the microhardness value, *HV*, was calculated using the following expression:

$$Hv = 1.854\frac{P}{d^2} \quad (3)$$

where P is the applied load (kg) and d denotes the arithmetic mean length as average of the two measured lengths of the two diagonals in mm. The indentation depth h was calculated using the following expression:

$$h = \frac{d}{7} \quad (4)$$

Microhardness measurements were performed with an applied load ranging from 0.01 to 0.2 kg. For each load, 10 measurements were taken. Subsequently, the dependence $Hv(h)$ was plotted. The error in the Hv was determined based on the statistical dispersion of the measurements.

3. Results and Discussion

The data from the XRD analysis indicated that aluminum and silicon were the main phases of the alloy before treatment (Figure 1). Additionally, diffraction peaks related to the phases Mg_5Si_6, Al_3FeSi_2, $Al_9(Fe,Mn)_3Si$ and $Al_3(Cu,Ni)_2$ were detected. The intensity of these phases was relatively low due to their small content in the sample volume. The presence of iron in the composition of silumin typically negatively affects the mechanical properties of the alloy due to the formation of brittle primary precipitates, Al_8Fe_2Si and Al_3FeSi_2 [5, 21,45]. To compensate for the negative effects of iron, manganese can be added to the alloy, resulting in the formation of $Al_9(FeMn)_3Si_2$ [5,46]. Another iron-containing phase detected by XRD in the original silumin, Al_3FeSi_2, is more characteristic of hypereutectic silumins [5]. Its presence in eutectic silumin may indicate an uneven casting composition and, consequently, a local excess of silicon concentration above the eutectic [47]. The formation of this phase in eutectic silumin has also been observed in the presence of additional alloying elements [45,48]. Alloying silumin with Cu and Ni results in the appearance of the $Al_3(Ni,Cu)_2$ phase, which was formed as a substitution solid solution based on Al_3Ni_2. In [5], it was noted that the formation of $Al_3(Ni,Cu)_2$ in industrial silumins is undesirable, as it depletes the aluminum matrix of copper atoms. The nonequilibrium crystallization of the silumin under study leads to the formation of a strengthening metastable phase Mg_5Si_6. Crystallization of the strengthening metastable phase Mg5Si6 in the studied silumin was also observed in a number of works on the study of the structure of Al-Si-Mg and Al-Si-Mg-Mn alloys [49,50].

Plasma treatment led to the disappearance of diffraction peaks for intermetallic and silicide phases (see Figure 1) as well as a decrease in intensity and broadening of the silicon diffraction peaks (insert in Figure 1).

The physical broadening of the silicon diffraction line can be attributed to the dispersion of both primary silicon crystals and silicon crystals in the Al-Si eutectic as well as the presence of residual mechanical stresses. The Williamson–Hall method was used to separate the contributions of these two factors (dispersion and stresses). According to this method, the mathematical relationship between the physical broadening of the diffraction line (β), the size of the coherent scattering blocks (D) and the microdeformations of the crystal lattice (ε) can be expressed as follows [51]:

$$\beta cos\theta = \frac{\lambda}{D} + 4\varepsilon sin\theta, \quad (1)$$

where θ is the diffraction angle at which the corresponding diffraction line is observed. The calculations showed that the size of the coherent scattering regions was 11 nm, and the value of microdeformation ε was ~0.4%. The appearance of residual microstrain may be associated with an increase in the density of dislocations due to the rapid cooling of the melt. In general, the appearance of microstress and, hence, microstrain in particles during crystallization under conditions of high cooling rates can be explained by an increase in dislocation density. However, such an interpretation warrants further investigation due

to the small size of Si particles (in the nano-scale range, as confirmed by TEM investigations). One could suggest that the strong disordering of the crystalline lattice of the silicon particles, formed at high cooling rates, could be the cause of this effect.

Since the intensity of the diffraction line is proportional to the amount of the analyzed substance, the decrease in silicon diffraction line intensity indicates a diminishing crystalline silicon content in the analyzed volume. The formation of a supersaturated substitutional solid solution based on aluminum, under conditions of ultrafast crystallization, is a possible reason for the decrease in silicon diffraction line intensity. According to the equilibrium phase diagram of Al-Si, the maximum solubility of silicon in the aluminum lattice is 1.59 at.% [5] at the crystallization temperature of the eutectic. Several studies [35,52,53] have shown that during crystallization under ultrafast cooling, some silicon atoms do not have enough time to solidify to primary crystals or eutectic, thus leading to an increase in silicon atom solubility in the aluminum lattice. Since the atomic radius of Si is 21.7% less than that of Al, the lattice parameter of the formed solid solution based on aluminum should be smaller than that of pure aluminum.

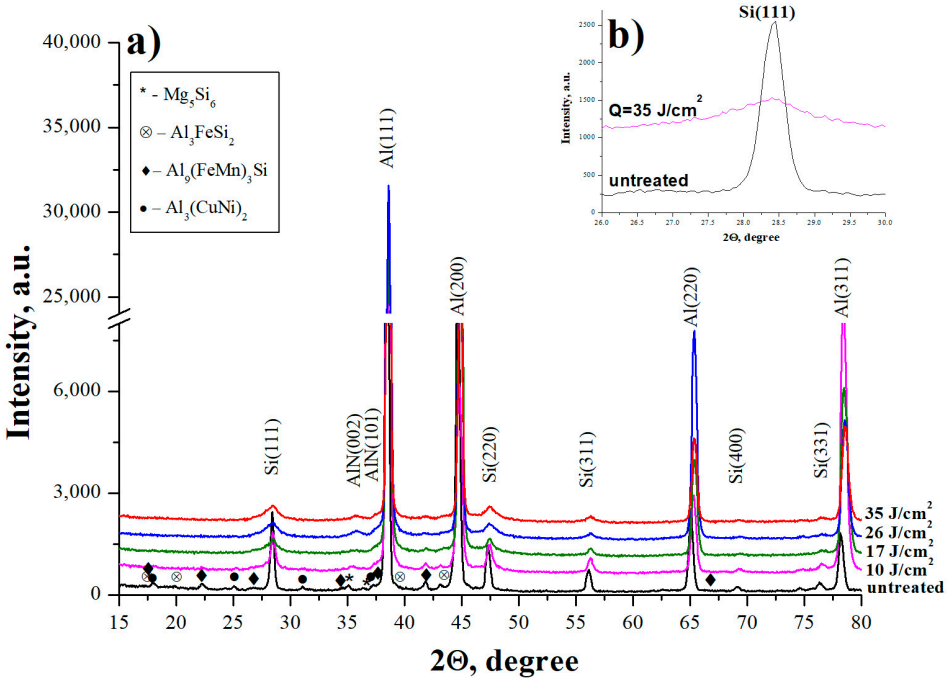

Figure 1. X-ray diffraction patterns of the samples: (**a**) - main drawing and (**b**) line Si(111).

an untreated silumin sample (**a**) and samples treated with CPF at different absorbed energy densities: (**b**) 10 J/cm²; (**c**) 17 J/cm²; (**d**) 26 J/cm² and **(e)** 35 J/cm².

Figure 2 illustrates the relationship between the aluminum lattice parameter, determined using the Al (311) line, and the absorbed energy density for the doped alloy. The data indicate that CPF treatment reduced the aluminum lattice parameter from 0.4050 ± 0.0004 nm in the initial samples to 0.4037 ± 0.0004 nm in the treated samples. The experimental relationship between the aluminum lattice parameter (d_{Al}) and silicon concentration (C_{Si}) is given in [35]

$$d_{Al}(\text{nm}) = 0.4049 - 1.63 \cdot 10^{-4} C_{Si}\ (\text{at.}\%), \quad (2)$$

This expression enables the estimation of the silicon concentration in the solid solution of aluminum for the binary alloy Al-Si. Calculations indicate that the Si concentration is expected to be around 6 at.% at an absorbed energy density of 35 J/cm^2.

However, the aluminum lattice parameter can also be influenced by other elements doped into the alloy. The results of the CPF treatment's effect on the lattice parameter of aluminum in the binary alloy (Al-12%Si) under the same processing conditions are illustrated in Figure 2 (pure Al-Si alloy). According to the obtained data, the aluminum lattice parameter is 0.4045 nm for the binary alloy (Al-12%Si), which is higher than that of the alloy doped with additional elements. The concentration of silicon in the solid solution of aluminum for the binary (Al-12%Si) alloy after CPF treatment is ~3 at.% according to formula (2).

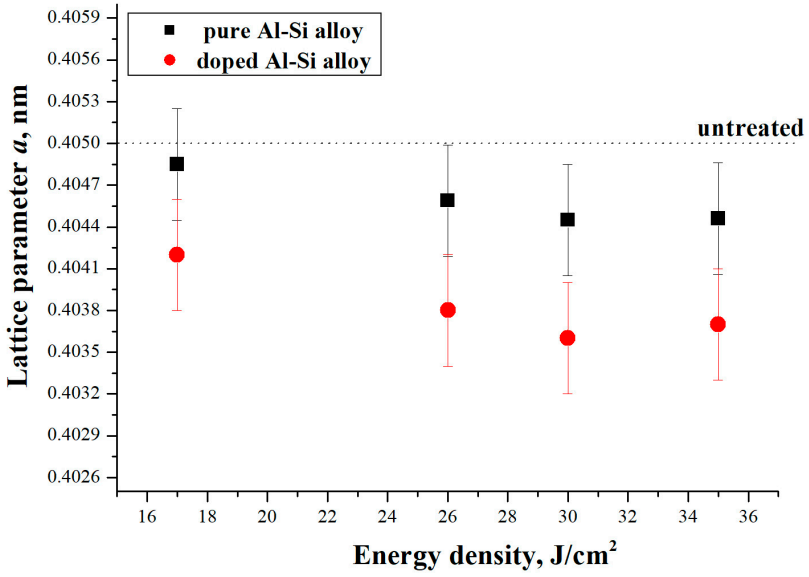

Figure 2. Variation of the aluminum lattice parameter with absorbed energy density.

A characteristic feature of compression plasma flows impacting materials is the potential for the surface layer to become saturated with atoms of the plasma-forming substance [54]. As a result of treatment with plasma flows generated in a nitrogen atmosphere, hexagonal closely packed (hcp) AlN formation was detected by XRD analysis (see Figure 1).

The investigation of the structure and elemental composition using scanning electron microscopy and energy-dispersive microanalysis revealed that the studied silumin in its initial state is significantly heterogeneous (Figure 3). Distinct crystallization regions of primary aluminum (region 1 in Figure 3a) and the crystallization regions of the Al-Si eutectic (region 2 in Figure 3a) can be identified based on differences in elemental composition and morphological features. According to EDX, the crystallization regions of primary aluminum contain 0.2–0.4 at.% Cu and 0.2–0.4 at.% Mg.

These elements exhibit high solubility in aluminum at room temperature. The eutectic region also contains magnesium, copper, nickel and iron, which can be part of both the aluminum-based solid solution and the finely dispersed intermetallic precipitates. Due to the presence of these elements, the eutectic regions appear light gray in the micrograph obtained using backscattered electrons. In addition to the finely dispersed intermetallics, the original silumin also contains coarse intermetallic and silicide precipitates of various compositions, as identified by XRD analysis (Figure 1). The size of these phases can reach several tens of micrometers.

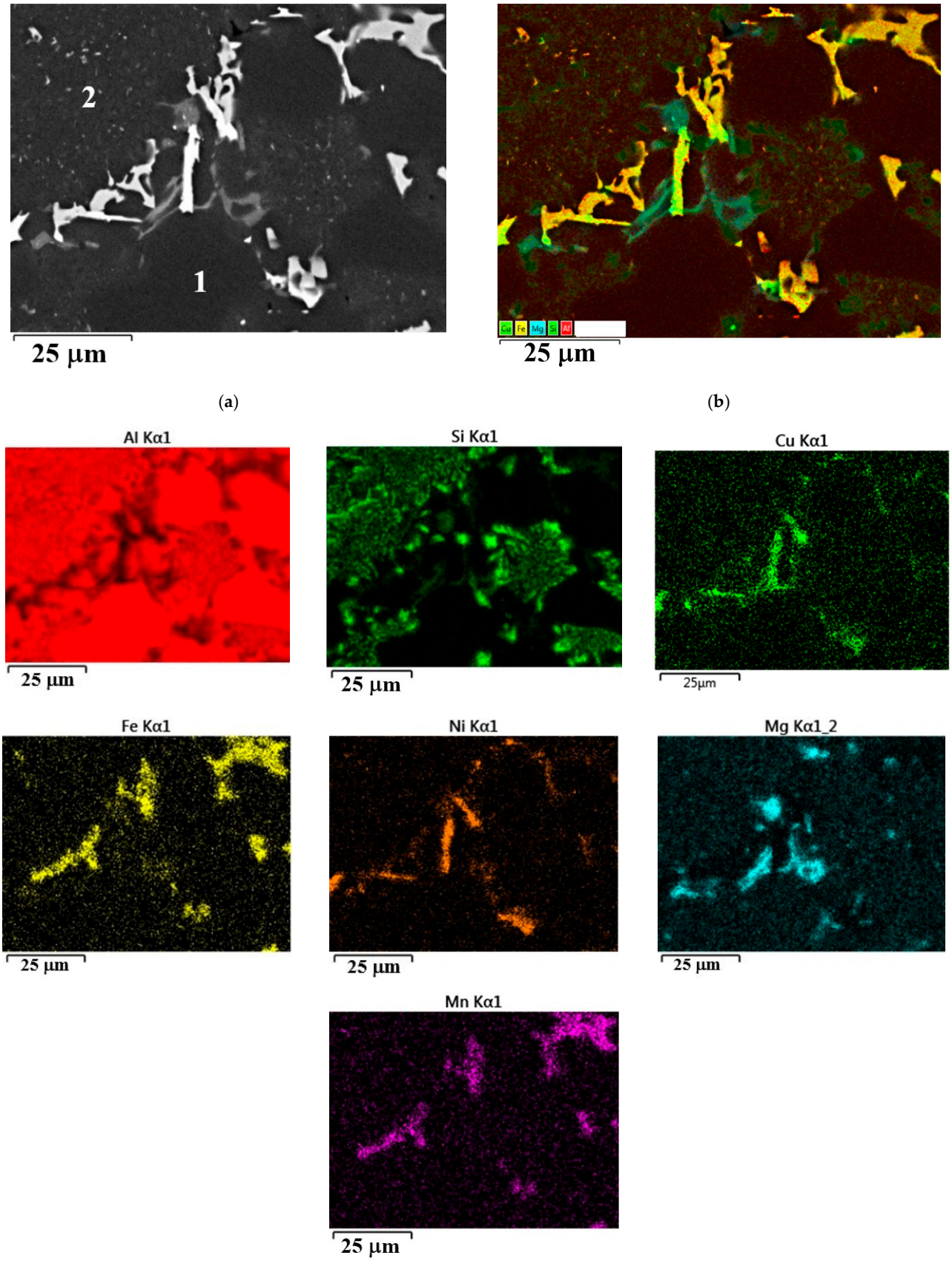

Figure 3. Microstructure of (**a**) the original silumin sample; (**b**) summarized elemental and (**c**) distributions of individual element.

The CPF impact on the studied silumin samples resulted in the formation of a modified near-surface layer, with its thickness, elemental composition and structure determined by the energy absorbed by the surface layer (Figure 4). The increase in absorbed energy density caused the molten layer thickness to grow from 5–10 μm at 10–17 J/cm² to 50 μm at 30–35 J/cm² (Figure 4b,c). A relatively uniform distribution of elements is observed in this layer after crystallization. The structure of the modified layer contains two sublayers, which were formed due to the uneven distribution of temperature along the depth and the different melting temperatures of the structural components of the studied alloy. The first sublayer (region I in Figure 4b,c) is located close to the surface of the sample. It is characterized by the melting of all structural components during CPF impact and an almost uniform distribution of all elements of the alloy (Figure 5).

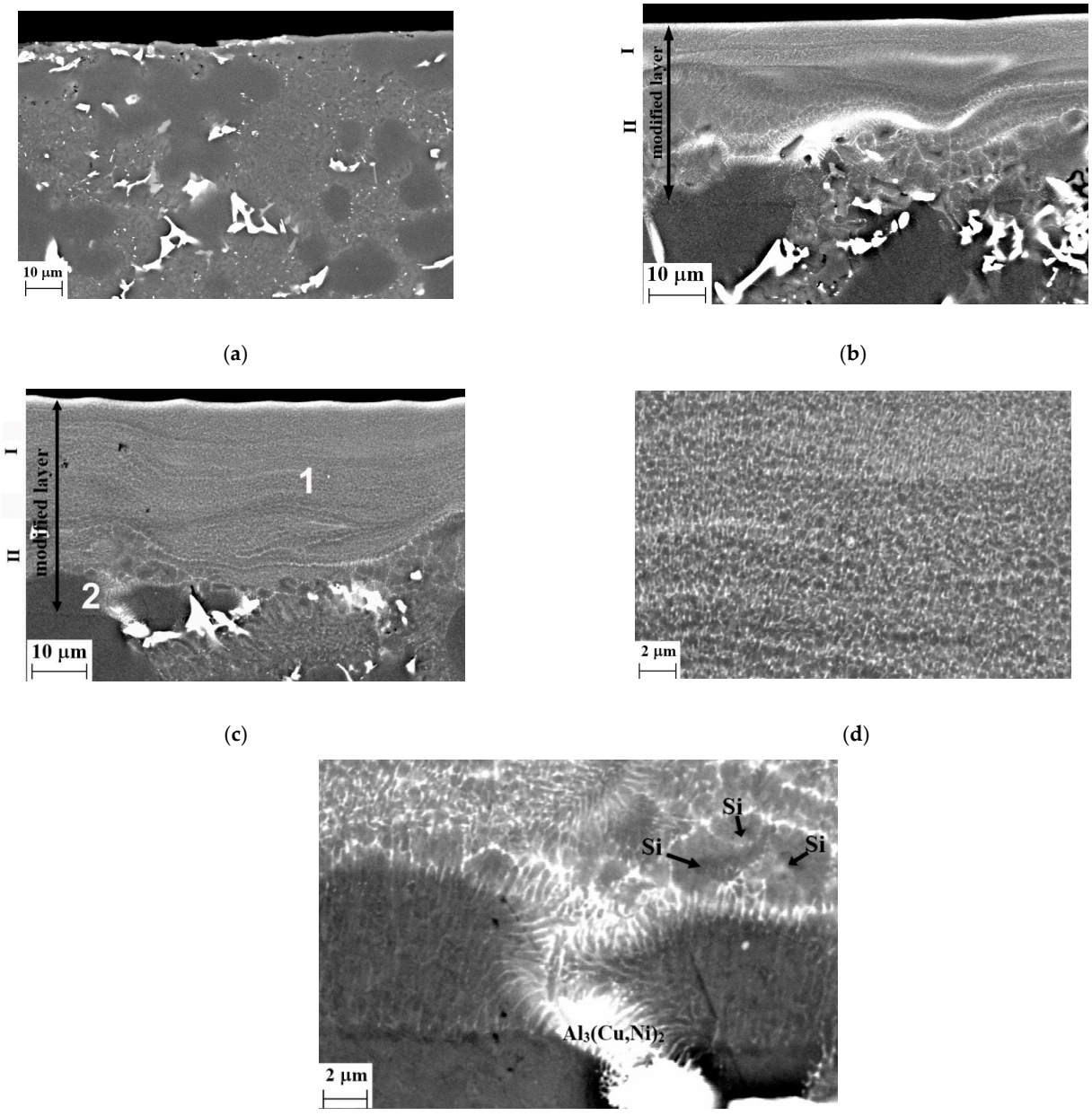

Figure 4. SEM images of silumin sample cross-sections: (**a**) untreated; (**b**) after CPF treatment at absorbed energy densities of 17 J/cm² and (**c–e**) 35 J/cm².

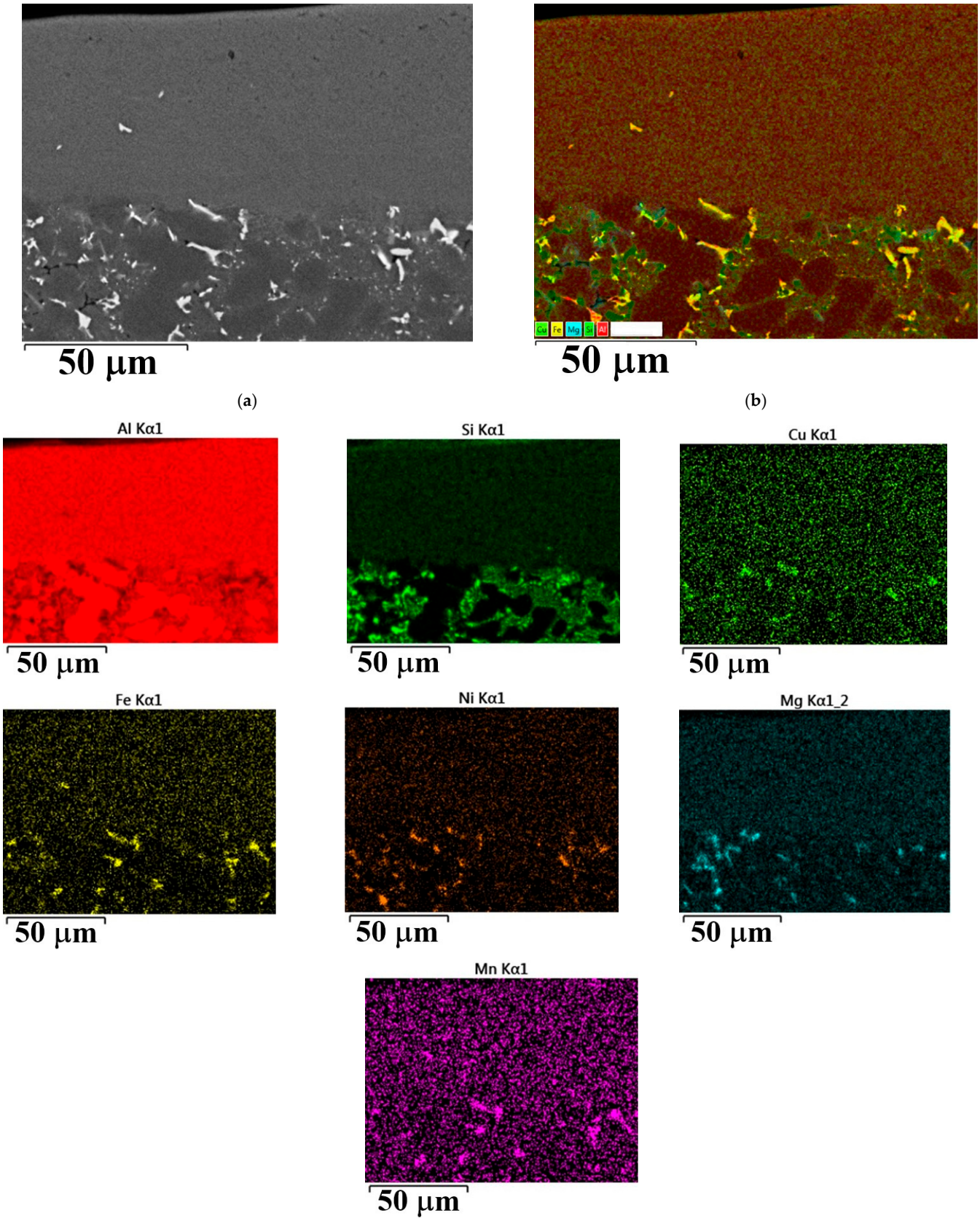

Figure 5. (**a**) Microstructure of the silumin sample cross-section, (**b**) summarized distribution of elements and (**c**) distributions of individual elements after plasma impact at 35 J/cm^2.

Convective liquid-phase mixing in the melt during plasma impact is the primary reason for the uniform distribution of elements. The first sublayer is characterized by a dispersed structure containing both equiaxed crystallites and crystallites with a specific growth direction (Figure 4e from area 1 in Figure 4c). The boundaries of the crystal exhibit a lighter elemental contrast, indicating an enrichment of the boundaries with alloying elements.

In the second underlying sublayer (region II in Figure 4b), the heat flux transferred to the sample as a result of plasma impact led to the melting of the aluminum matrix and eutectic; however, the energy transferred to this layer is insufficient for the complete dissolution of the intermetallic and silicide phases as well as silicon precipitates (see Figure 4e from area 2 in Figure 4c). Unmelted precipitates in this sublayer act as local heat sinks, thereby increasing the cooling rate in these areas and causing the formation of columnar dendritic crystals [55,56].

Transmission electron microscopy was used for a more detailed study of the modified layer structure. A lamella oriented perpendicular to the surface was cut from the sample treated with plasma at Q = 35 J/cm² using a focused ion beam (Figure 6a). The length of the studied lamella was 10 μm, and its thickness was 70–80 nm.

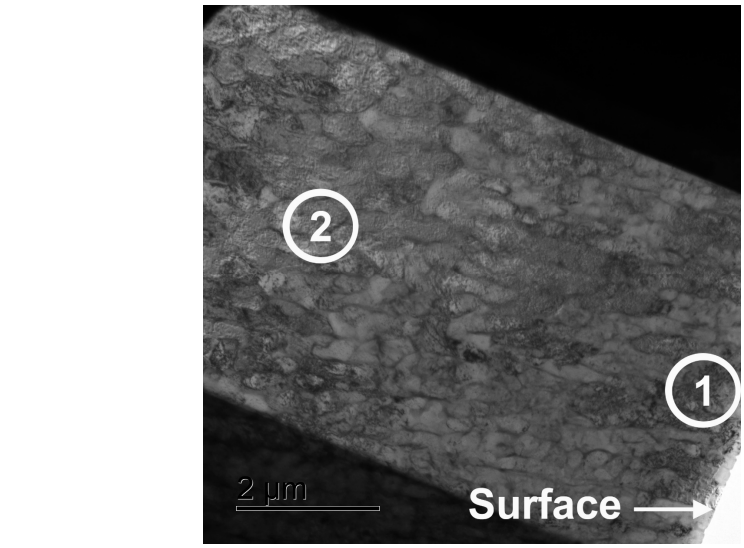

(**a**)

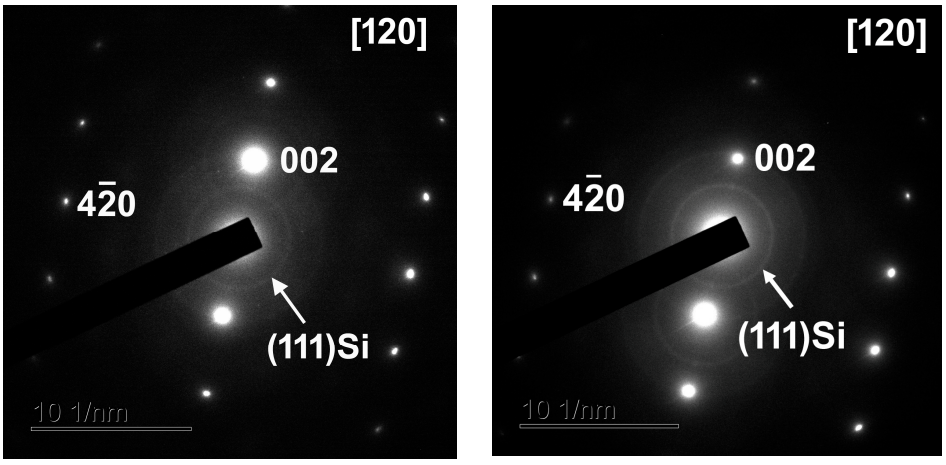

(**b**) (**c**)

Figure 6. (**a**) Bright-field image of the sample treated with CPF at 35 J/cm²; (**b**) corresponding SAED pattern from local areas marked as 1; (**c**) corresponding SAED pattern from local area marked as 2.

The characteristic SAED patterns from different areas of the bright-field image were consistent, representing point diffraction patterns from aluminum solid solution grains and varying rings from dispersed silicon crystallites, each with different orientations relative to the analyzing electron beam (Figure 6b,c). The resulting SAED patterns corresponded to the [120] zone axis, which is the crystallographic axis oriented perpendicular to the studied area of the sample. The uniformity of the diffraction patterns from various areas indicates consistent orientation of aluminum grain growth from the melt during the cooling of the surface layer.

An area of the studied lamella at higher magnification is shown in Figure 7. It is evident from the figure that aluminum grains are predominantly elongated along the axis perpendicular to the surface. The grain size varies within the range of 100–500 nm, which corresponds to the size of the aluminum crystallites observed using the SEM method (see Figure 4d). A comparison of the diffraction patterns (see Figure 6b,c) and the grain structure shown in Figure 6 allows us to conclude that the grains are primarily oriented along the crystallographic <100> direction, which corresponds to their growth during crystallization. The preferential growth in the <100> direction under conditions of high-speed cooling from the melt is typical of materials with a face-centered cubic lattice [57]. This <100> direction provides the maximum growth rate of the crystal when aligned closely with the direction of the heat sink during high-speed cooling [58].

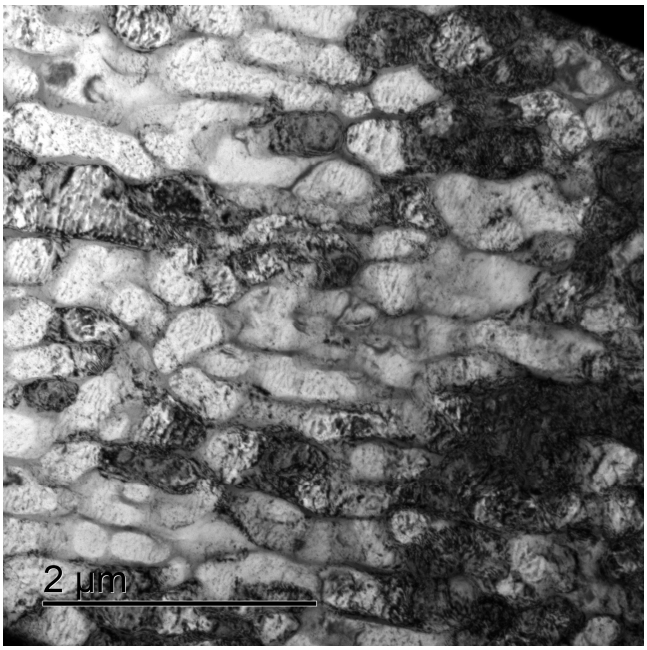

Figure 7. Bright-field image of a local area of the sample treated with CPF at 35 J/cm^2.

It should be noted that no significant change in texture was detected in the X-ray diffraction patterns after treatment (see Figure 1). This lack of change may be attributed to the fact that X-ray analysis examines a layer with a thickness of ~30 μm; i.e., the diffraction patterns are averaged over the entire thickness of the analyzed layer.

The distribution of silicon crystallites in the surface layer modified by plasma impact was also studied. Figure 8 presents a dark-field image of the structure formed by selecting silicon diffraction rings along with the corresponding bright-field image.

From the figure, it is evident that silicon crystallites form as nanoscale precipitates in the interlayer between the grains of the aluminum solid solution. The size of the silicon crystallites is consistent with the value obtained by XRD, which is several tens of nanometers.

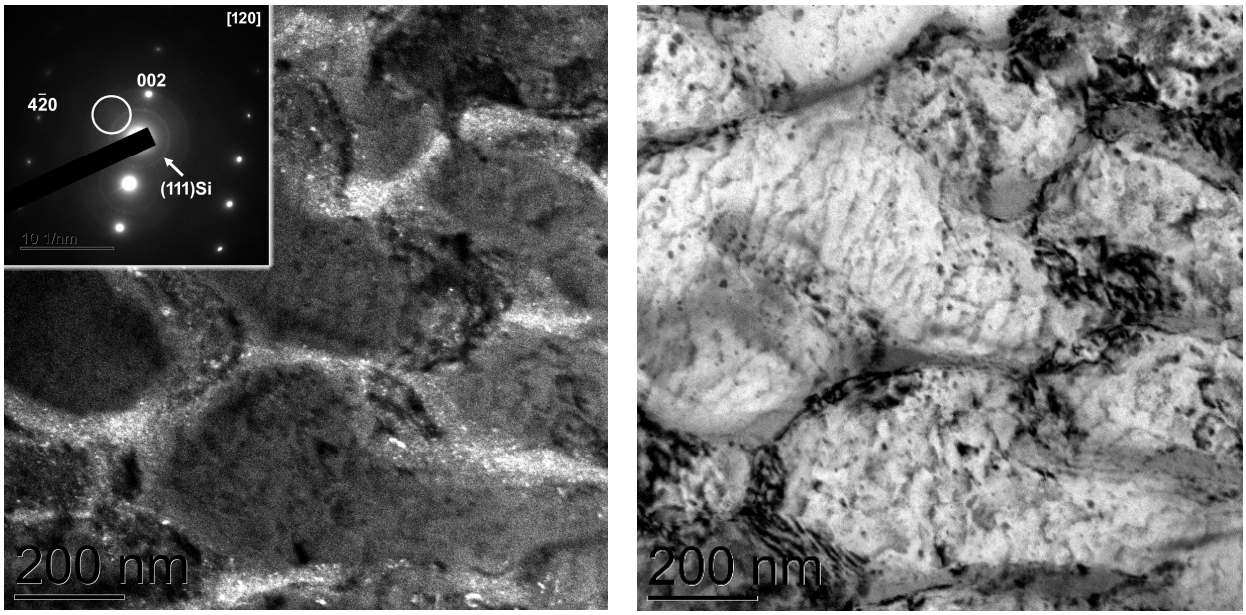

(**a**) (**b**)

Figure 8. (**a**) Dark-field image produced selecting Si diffraction rings; (**b**) corresponding bright-field image of local area of sample treated with CPF at 35 J/cm^2.

Table 1 shows the composition of different regions (inside the solid solution grains, and in the interlayer between the grains, at the grain–interlayer boundary) designated by the corresponding numbers in the bright-field image in Figure 9. A comparison of the table and figure data indicates that the silicon concentration inside the grains corresponds to ~3 at.% Si (areas 1 and 3), which correlates with the data presented in Figure 2. This suggests that the central part of the grains consists of a supersaturated solid solution of ~3 at.% silicon in aluminum. The solid solution may also contain other alloying elements at concentrations lower than the detection limit of energy-dispersive microanalysis. The table indicates that the remaining silicon, along with other alloying elements, is carried by the crystallization front to the boundaries of the growing grain, forming an interlayer between the grains. The boundaries of the grains are enriched with silicon and magnesium (areas 4 and 5). The interlayer, in addition to aluminum and silicon, contains nickel, magnesium, iron and manganese (area 6). The composition of the interlayer corresponds to a hypereutectic alloy of aluminum, in which nanosized silicon precipitates are formed (see Figure 8). This interlayer creates a rigid framework around the grains of the supersaturated solid solution of aluminum with silicon, enhancing the strength characteristics of the surface layer.

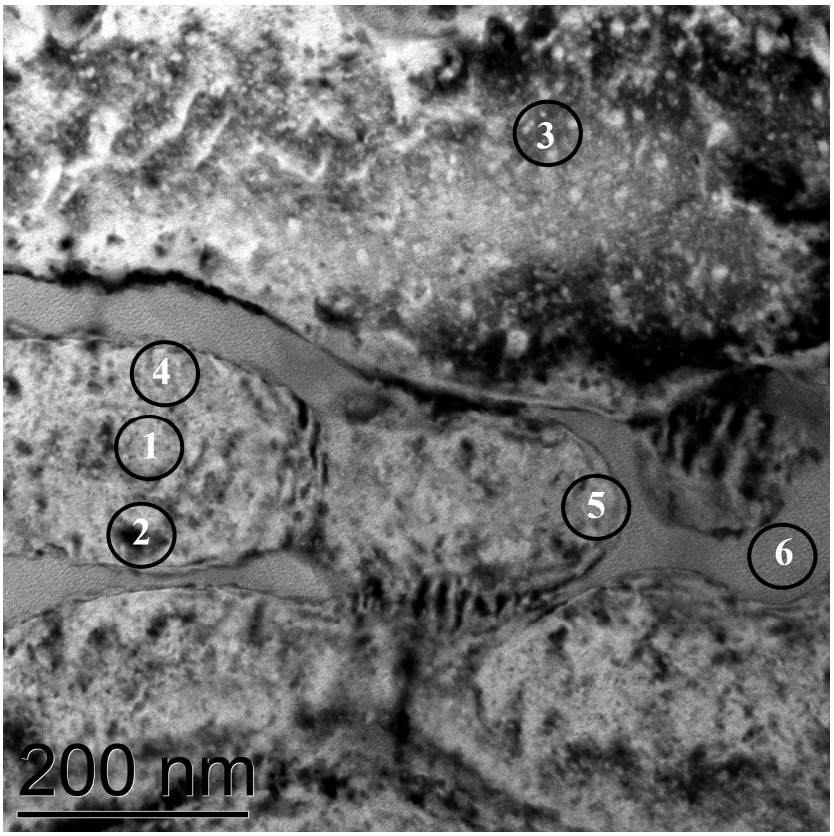

Figure 9. Bright-field image of the sample treated with CPF at 35 J/cm^{2,} with corresponding areas showing different compositions as listed in Table 1.

Table 1. Composition (at.%) of areas marked in Figure 9 by a ring (size of diaphragm).

Area	Al	Si	Mg	Ni	Mn	Fe
1	97.3	2.7	-	-	-	-
2	96.9	3.2	-	-	-	-
3	96.2	3.8	-	-	-	-
4	96.6	3.1	0.3	-	-	-
5	82.0	15.1	1.3	-	-	-
6	33.6	52.0	4.6	6.5	1.2	2.2

Structural-phase transformations in the surface layer caused changes in the strength properties of the studied alloy (Figure 10). The microhardness of the untreated alloy was 130 Hv. CPF treatment increased the microhardness of the surface layer, reaching a value of 205 Hv at a depth of 1.5 μm before decreasing to ~180 Hv at greater depths following treatment at 35 J/cm^2 (Figure 10). For samples treated at lower absorbed energy densities, the maximum microhardness of the modified layer ranged from 170 to 180 Hv. The microhardness of the treated samples at greater depths remained higher than that of the untreated samples. The increase in microhardness at lower indentation loads (closer to the surface) can be attributed to the formation of AIN during plasma impact.

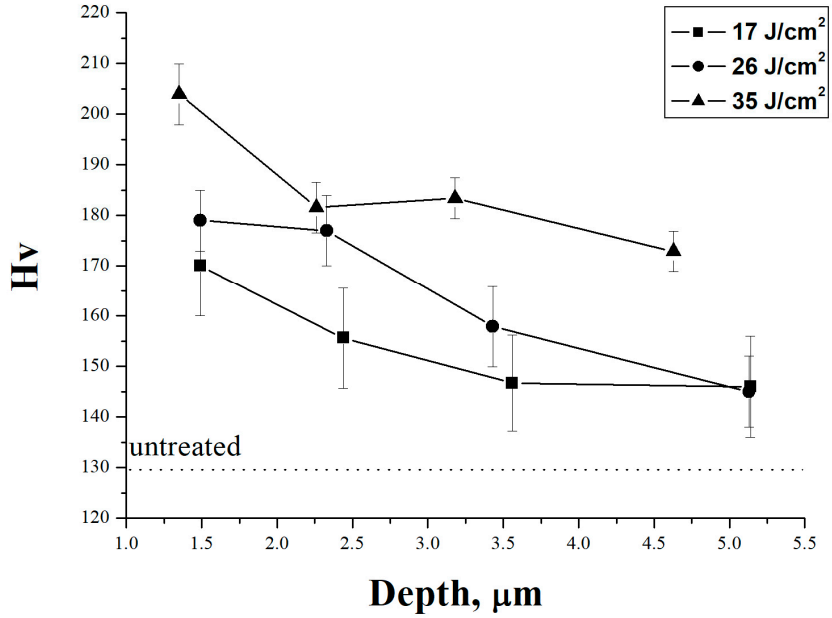

Figure 10. Dependence of microhardness on the indentation depth of the silumin sample treated with CPF at different absorbed energy densities.

Four primary mechanisms for materials strengthening are well established: solid solution strengthening, precipitation hardening, grain boundary strengthening and strain hardening [59]. Based on the studies of the silumin structure after the CPF impact discussed in this paper, it is evident that all of these mechanisms contribute to silumin strengthening. Let us consider the influence of each mechanism on microhardness in the bulk of the treated layer (at a higher indentation depth) and the increase in microhardness at 35 J/cm² (at a depth of 4.5 μm).

Solid-solution strengthening after the plasma treatment of silumin is primarily associated with the formation of a supersaturated Al (Si) solid solution. However, as illustrated in Figure 2, the aluminum lattice parameter changes remain within the error limits. Thus, it can be concluded that while the solid-solution mechanism can influence the microhardness of the samples after CPF impact, it is not the primary mechanism explaining the increase in microhardness at 35 J/cm².

The increase in microhardness due to precipitation hardening can be attributed to the formation of nanosized silicon inclusions in the interlayers between Al (Si) solid solution grains. However, the estimated size of these nanosized silicon crystals obtained from XRD analysis for samples processed at different absorbed energy densities remains nearly the same.

The grain boundary strengthening mechanism can be estimated from the Hall–Petch relationship [60]:

$$\sigma = \sigma_0 + \frac{k}{\sqrt{d}} \quad (1)$$

where σ_0 and k are constants, and d represents the average grain diameter. It has been shown that plasma impact refines the grain structure of both aluminum and silicon as well as intermetallic precipitates. An increase in the energy absorbed by the surface layer leads to a higher cooling rate during crystallization, thereby reducing grain sizes. This mechanism could explain the observed effects. However, the constant k for pure aluminum (0.06–0.28 MPa mm1/2 [61,62]) is much smaller than that of other metallic materials, such as mild steel (23.4 MPa mm1/2 [62]) or pearlitic steel (~19.7 MPa mm1/2 [62]).

Strain hardening may increase microhardness at Q = 35 J/cm²; however, the evolution of the defect structure was not investigated in this study. Several prior investigations [63,64] demonstrated that a higher cooling rate during crystallization from the melt leads to increased dislocation density and, consequently, improved strength characteristics.

4. Conclusions

1. The investigations show that compression plasma flows impacting eutectic silumin alloy cause the melting of the alloy's surface layer, homogenization of its composition and subsequent crystallization.
2. Melting results in the dissolution of intermetallic compounds and primary silicon crystals within the surface layer.
3. The thickness of the molten (modified) layer increases with the density of absorbed energy, ranging from 5–10 μm at 10–17 J/cm² to 50 μm at 30–35 J/cm². The modified layer consists of two sublayers formed due to uneven temperature distribution during plasma treatment.
4. A supersaturated solid solution of silicon in aluminum is observed in the modified layer, resulting in a decrease in the aluminum lattice parameter after plasma treatment.
5. Aluminum nitride forms at the alloy's surface due to the diffusion of nitrogen from the residual atmosphere of the vacuum chamber.
6. Transmission electron microscopy analysis showed that the silicon concentration in the center of the aluminum-based solid solution is ~3 at.%. The boundaries of the grains are enriched with silicon and magnesium.
7. The interlayer between grains is enriched with alloying elements. Its composition corresponds to a hypereutectic aluminum alloy in which nanosized silicon precipitates form.
8. Plasma impact results in an increase in microhardness from 130 to 205 Hv. A greater energy density absorbed by the surface layer leads to increased microhardness.

Author Contributions: Conceptualization, N.B. and N.C.; methodology, N.B., N.C., V.A., A.K. and A.M.; resources A.M.; investigation, N.B, N.C., C.S., V.A., A.K. and Y.M.; data curation, N.B., N.C., A.M., V.A., Y.M. and A.V.; supervision, N.C., A.M. and A.V.; writing—original draft preparation, N.B. and N.C.; writing—review and editing, N.B., N.C., C.S., Y.M. and A.V.; project administration, N.B. and A.M.; funding acquisition, A.M. All authors have read and agreed to the published version of the manuscript.

Funding: This research was funded by the Russian Science Foundation under project (No. 23-19-00517).

Data Availability Statement: The original contributions presented in this study are included in the article. Further inquiries can be directed to the corresponding author.

Acknowledgments: The study used the equipment from the Centre for collective use of Moscow State University of Technology "STANKIN" (agreement No. 075-15-2021-695, 26/07/2021).

Conflicts of Interest: The authors declare no conflicts of interest.

References

1. Ashkenazi, D. How aluminum changed the world: A metallurgical revolution through technological and cultural perspectives. *Technol. Forecast. Soc. Change* **2019**, *143*, 101–113.
2. Sarıkaya, M.; Başcıl Önler, D.; Dağlı, S.; Hartomacıoğlu, S.; Günay, M.; Królczyk, G.M. A review on aluminum alloys produced by wire arc additive manufacturing (WAAM): Applications, benefits, challenges and future trends. *J. Mater. Res. Technol.* **2024**, *33*, 5643–5670.
3. Song, C.-R.; Dong, B.-X.; Zhang, S.-Y.; Yang, H.-Y.; Liu, L.; Kang, J.; Meng, J.; Luo, C.-J.; Wang, C.-G.; Cao, K.; et al. Recent progress of Al–Mg alloys: Forming and preparation process, microstructure manipulation and application. *J. Mater. Res. Technol.* **2024**, *31*, 3255–3286.

4. Gao, Y.-C.; Dong, B.-X.; Yang, H.-Y.; Yao, X.-Y.; Shu, S.-L.; Kang, J.; Meng, J.; Luo, C.-J.; Wang, C.-G.; Cao, K.; et al. Research progress, application and development of high performance 6000 series aluminium alloys for new energy vehicles. *J. Mater. Res. Technol.* **2024**, *32*, 1868–1900.
5. Zolotorevsky, V.S.; Belov, N.A.; Glazoff, M.V. *Casting Aluminium Alloys*; Elsevier Ltd.: Amsterdam, The Netherlands, 2007; ISBN 9780080550237.
6. Abdelaziz, M.H. Effect of additives on the microstructure and tensile properties of Al–Si alloys. *J. Mater. Res. Technol.* **2019**, *8*, 2255–2268.
7. Konovalov, S.; Zaguliaev, D.; Ivanov, Y.; Gromov, V.; Abaturova, A. Modification of Al-10Si-2Cu alloy surface by intensive pulsed electron beam. *J. Mater. Res. Technol.* **2020**, *9*, 5591–5598.
8. Lipinski, T. The Influence of the Proportions of Titanium and Boron in the Al and AlSi7-Based Master Alloy on the Microstructure and Mechanical Properties of Hypoeutectic Silumin AlSi7Mg. *Appl. Sci*. **2023**, *13*, 12590.
9. Student, M.; Pohrelyuk, I.; Padgurskas, J.; Posuvailo, V.; Hvozdets'kyi, V.; Zadorozhna, K.; Chumalo, H.; Veselivska, H.; Kovalchuk, I.; Kychma, A. Influence of Plasma Electrolytic Oxidation of Cast Al-Si Alloys on Their Phase Composition and Abrasive Wear Resistance. *Coatings* **2023**, *13*, 637.
10. Zykova, A.; Martyushev, N.; Skeeba, V.; Zadkov, D.; Kuzkin, A. Influence of W Addition on Microstructure and Mechanical Properties of Al-12%Si Alloys. *Materials* **2019**, *12*, 981.
11. Lipinski, T. Effect of Al5TiB Master Alloy with P on Microstructure and Mechanical Properties of AlSi7Mg Alloy. *Metals* **2023**, *13*, 1560.
12. Godbole, K.; Bhushan, B.; Narayana Murty, S.V.S.; Mondal, K. Al-Si controlled expansion alloys for electronic packaging applications. *Prog. Mater. Sci.* **2024**, *144*, 101268.
13. Arriaga-Benitez, R.I.; Pekguleryuz, M. Recent Progress in Creep-Resistant Aluminum Alloys for Diesel Engine Applications: A Review. *Materials* **2024**, *17*, 3076.
14. Liu, Y.; Xiong, S. Research Progress on Thermal Conductivity of High-Pressure Die-Cast Aluminum Alloys. *Metals* **2024**, *14*, 370.
15. Zhang, L.; Ji, Z.-W.; Zhao, J.; He, J.; Jiang, H. Factors affecting eutectic Si modification in Al-Si hypoeutectic alloy with the addition of Na, Sr, Eu and Yb. *Mater. Lett.* **2022**, *308*, 131206.
16. Fatahalla, N.; Hafiz, M.; Abdulkhalek, M. Effect of microstructure on the mechanical properties and fracture of commercial hypoeutectic Al–Si alloy modified with Na, Sb and Sr. *J. Mater. Sci.* **1999**, *34*, 3555–3564.
17. Luna, I.A.; Molinar, H.M.; Castro Román, M.J.; Escobedo Bocardo, J.C.; Trejo, M.H. Improvement of the tensile properties of an Al–Si–Cu–Mg aluminum industrial alloy by using multi stage solution heat treatments. *Mater. Sci. Eng. A* **2013**, *561*, 1–6.
18. Nowak, B.M.; Babu, N.H. Grain refinement of Al–Si alloys by Nb–B inoculation. Part II: Application to commercial alloys. *Mater. Des.* **2015**, *66*, 376–383.
19. Kakitania, R.; Rodriguesa, A.V.; Silva, C.; Garcia, A.; Cheung, N. The roles of solidification cooling rate and (Mn, Cr) alloying elements in the modification of β-AlFeSi and hardness evolvements in near-eutectic Al-Si alloys. *J. Alloys Metall. Syst.* **2023**, *1*, 100005.
20. Knipling, K.K.; Dunand, D.C.; Seidman, D.N. Criteria for developing castable, creep-resistant aluminum-based alloys—A review. *Int. J. Mat. Res.* **2006**, *97*, 246–265.
21. Piatkowski, J.; Roskosz, S.; Sapota, W.; Stach, S. The Influence of Iron Content on the Porosity of AlSi9 Alloy Intended for Alfining Piston Ring Inserts. *Materials* **2024**, *17*, 5181.
22. Lipinski, T. Effect of Modifier Form on Mechanical Properties of Hypoeutectic Silumin. *Materials* **2023**, *16*, 5250.
23. Zaguliaev, D.; Konovalov, S.; Ivanov, Y.; Gromov, V.; Petrikova, E. Microstructure and mechanical properties of doped and electron-beam treated surface of hypereutectic Al-11.1%Si alloy. *J. Mater. Res. Technol*. **2019**, *8*, 3835–3842.
24. Koval, N.N.; Koval, T.V.; Krysina, O.V.; Ivanov, Y.F.; Teresov, A.D.; Moskvin, P.V.; Tran, M.K.A.; Prokopenko, N.A.; Petrikova, E.A. Experimental Study and Mathematical Modeling of the Processes Occurring in ZrN Coating/Silumin Substrate Systems under Pulsed Electron Beam Irradiation. *Coatings* **2021**, *11*, 1461.
25. Ivanov, Y.; Gromov, V.; Zaguliaev, D.; Glezer, A.; Sundeev, R.; Rubannikova, Y.; Semin, A. Modification of surface layer of hypoeutectic silumin by electroexplosion alloying followed by electron beam processing. *Mater. Lett.* **2019**, *253*, 55–58.
26. Ivanov, Y.; Zaguliaev, D.; Glezer, A.; Gromov, V.; Abaturova, A.; Leonov, A.; Semin, A.; Sundeev, R. Changes in surface structure and mechanical characteristics of Al–5 wt% Si alloy after irradiation by electron beam. *Mater. Lett*. **2020**, *275*, 128105.
27. Ustinov, A.; Klopotov, A.; Ivanov, Y.; Zagulyaev, D.; Teresov, A.; Petrikova, E.; Gurianov, D.; Chumaevskii, A. Deformation Inhomogeneities of a Hypoeutectic Aluminium-Silicon Alloy Modified by Electron Beam Treatment. *Materials* **2023**, *16*, 2329.
28. Zagulyaev, D.; Konovalov, S.; Gromov, V.; Glezer, A.; Ivanov, Y.; Sundeev, R. Structure and properties changes of Al-Si alloy treated by pulsed electron beam. *Mater. Lett.* **2018**, *229*, 377–380.
29. Zaguliaev, D.V.; Konovalov, S.V.; Ivanov, Y.F.; Gromov, V.E.; Shlyarov, V.V.; Rubannikova, Y.A. The Effect of High-Intensity Electron Beam on the Crystal Structure, Phase Composition, and Properties of Al–Si Alloys with Different Silicon Content. *Prog. Phys. Met.* **2021**, *22*, 129–157.
30. Abbas, M.K.; Mahmoud, A.K. Laser surface treatment of Al-12%Si alloy. *Mater. Today* **2017**, *4*, 9992–9996.
31. You, M.-L.; Li, S.-M.; Shi, Z.-Z. Significant hardness improvement of a low-density Al-Si-Mg-Li-Fe alloy through laser-aging surface treatment. *Mater. Today Commun.* **2022**, *32*, 104000.

32. Tomida, S.; Nakata, K.; Shibata, S.; Zenkouji, I.; Saji, S. Improvement in wear resistance of hyper-eutectic Al–Si cast alloy by laser surface remelting. *Surf. Coat. Technol.* **2003**, *169–170*, 468–471.
33. Pauleau, Y. *Materials Surface Processing by Directed Energy Techniques*; Elsevier: Amsterdam, The Netherlands, 2006; p. 722.
34. Zaguliaev, D.V.; Klopotov, A.A.; Ivanov, Y.F.; Ustinov, A.M.; Abzaev, Y.A.; Teresov, A.D. Electron beam modification of the structure and properties of silumins with various silicon concentrations. *J. Phys. Conf. Ser.* **2021**, *2064*, 012081.
35. Akamatsu, H.; Tanaka, H.; Yamanishi, T.; Egawa, S.; Yamasaki, T.; Miki, M.; Yatsuzuka, M. Increase of Si solution rate into Al matrix by repeated irradiation of intense pulsed ion beam. *Vacuum* **2002**, *65*, 563–569.
36. Grigoriev, S.; Vereschaka, A.; Milovich, F.; Sitnikov, N.; Seleznev, A.; Sotova, C.; Bublikov, J. Influence of the yttrium cathode arc current on the yttrium content in the (Ti, Y, Al) N coating and the coating properties. *Vacuum* **2024**, *222*, 113028.
37. Grigoriev, S.; Vereschaka, A.; Milovich, F.; Migranov, M.; Andreev, N.; Bublikov, J.; Sitnikov, N.; Oganyan, G. Investigation of the tribological properties of Ti-TiN-(Ti,Al,Nb,Zr)N composite coating and its efficiency in increasing wear resistance of metal cutting tools. *Tribol. Int.* **2021**, *164*, 107236.
38. Vereschaka, A.; Grigoriev, S.; Milovich, F.; Sitnikov, N.; Migranov, M.; Andreev, N.; Bublikov, J.; Sotova, C. Investigation of tribological and functional properties of Cr,Mo-(Cr,Mo)N-(Cr,Mo,Al)N multilayer composite coating. *Tribol. Int.* **2021**, *155*, 106804.
39. Purić, J.; Dojčinović, I.P.; Astashynski, V.M.; Kuraica, M.M. Diagnostics of magnetoplasma compressor of compact geometry. *Publ. Astron. Obs. Belgrade*. **2003**, *76*, 85–104.
40. Dojčinović, I.P.; Kuraica, M.M.; Obradović, B.M.; Cvetanović, N.; Purić, J. Optimization of plasma flow parameters of the magnetoplasma compressor. *Plasma Sources Sci. Technol*. **2007**, *16*, 72–79.
41. Cherenda, N.N.; Leyvi, A.Y.; Petuh, A.; Uglov, V.V. Modification of Ti-6Al-4V titanium alloy surface relief by compression plasma flows impact. *High Temp. Mater. Process.* **2024**, *28*, 7–24.
42. Shymanski, V.I.; Jevdokimovs, A.; Cherenda, N.N.; Astashynski, V.M.; Petrikova, E.A. Structure and phase composition of hypereutectic silumin alloy Al-20Si after compression plasma flows impact. *J. Belarus. St. Univ. Phys*. **2021**, *2*, 25–33.
43. Cherenda, N.N.; Basalai, A.V.; Uglov, V.V.; Laskovnev, A.P.; Astashynski, V.M.; Kuzmitski, A.M. Phase composition and mechanical properties of Cu-Ti alloys synthesized in the surface layer of copper by plasma impact on the Ti/Cu system. *Vacuum* **2019**, *167*, 452–458.
44. Cherenda, N.N.; Basalai, A.V.; Shymanski, V.I.; Uglov, V.V.; Astashynski, V.M.; Kuzmitski, A.M.; Laskovnev, A.P.; Remnev, G.E. Modification of Ti-6Al-4V alloy element and phase composition by compression plasma flows impact. *Surf. Coat. Technol.* **2018**, *355*, 148–154.
45. Ebhota, W.; Jen, T. Intermetallics Formation and Their Effect on Mechanical Properties of Al-Si-X Alloys. *Intermet. Compd.-Form. Appl.* **2018**, *5*, 21–41.
46. Toscano, J.A.G.; Flores, A.V.; Salinas, A.R.; Nava, E.V. Microstructure of $Al_9(MnFe)_xSi$ intermetallics produced by pressure-assisted reactive sintering of elemental AlMnFeSi powder mixtures. *Mater. Lett.* **2003**, *57*, 2246–2252.
47. Kral, M.V.; Nakashima, P.N.H.; Mitchell, D.R.G. Electron Microscope Studies of Al-Fe-Si Intermetallics in an Al-11 Pct Si Alloy. *Metall. Mater. Trans. A* **2006**, *37A*, 1987–1997.
48. Lacaze, J.; Eleno, L.; Sundman, B. Thermodynamic assessment of the aluminum corner of the Al-Fe-Mn-Si system. *Metall. Mater. Trans. A* **2010**, *41*, 2208–2215.
49. Qian, X.; Wang, G.; Li, Y.; Wang, Y.; Peng, Y. Formation mechanism of β″-Mg5Si6 and its PFZ in an Al-Mg-Si-Mn alloy: Experiment and first-principles calculations. *Mater. Charact.* **2022**, *197*, 112617. https://doi.org/10.1016/j.matchar.2022.112617.
50. Wang, Y.; Liu, Z.K.; Chen, L.Q.; Wolverton, C. First-principles calculations of β″-Mg5Si6/α-Al interfaces. *Acta Mater.* **2007**, *55*, 5934–5947.
51. Suryanarayana, C.; Norton, M.G.; Suryanarayana, C.; Norton, M.G. *X-ray Diffraction*; Springer: New York, NY, USA, 1998; Practical aspects of X-ray diffraction; pp. 63–94.
52. Hao, Y.; Gao, B.; Tu, G.F.; Li, S.W.; Hao, S.Z.; Dong, C. Surface modification of Al-20Si alloy by high current pulsed electron beam. *Appl. Surf. Sci*. **2011**, *257*, 3913–3919.
53. Uzuna, O.; Karaaslan, T.; Gogebakan, M.; Keskin, M. Hardness and microstructural characteristics of rapidly solidified Al–8–16 wt.%Si alloys. *J. Alloys Compd*. **2004**, *376*, 149–157.
54. Cherenda, N.N.; Shimanskii, V.I.; Uglov, V.V.; Astashinskii, V.M.; Ukhov, V.A. Nitriding of steel and titanium surface layers under the action of compression plasma flows. *J. Surf. Investig.* **2012**, *6*, 319–325.
55. Gulyaev, A.P. *Metal Science and Heat Treatment*; Springer: Berlin/Heidelberg, Germany, 1994. https://doi.org/10.1007/BF01398077.
56. Chalmers, B. *Principles of Solidification*; R.E. Krieger Publishing Company: Malabar, FL, USA, 1977; p. 319.
57. Harris, G.B. Quantitative measurement of preferred orientation in rolled uranium bars. *Phil. Mag.* **1952**, *43*, 113–123.
58. *Physical Metallurgy*; Ed. Cahn, R.W., Haasen, P.; Elsevier: Amsterdam, The Netherlands, 1996; Volume 2.
59. Mirkin, L.I. *Physical Foundations of Strength and Plasticity*; Publishing House of Moscow State University: Moscow, Russia, 1968.
60. Hansen, N. Hall–Petch relation and boundary strengthening. *Scripta Materialia* **2004**, *51*, 801–806.
61. Thangaraju, S.; Heilmaier, M.; Murty, B.S.; Vadlamani, S.S. On the Estimation of True Hall–Petch Constants and Their Role on the Superposition Law Exponent in Al Alloys. *Adv. Eng. Mater.* **2012**, *14*, 892–897.
62. Armstrong, R.W. Crystal Engineering for Mechanical Strength at Nano-Scale Dimensions. *Crystals* **2017**, *7*, 315.

63. Krasnikov, V.S.; Mayer, A.E. Numerical investigation of the change of dislocation density and microhardness in surface layer of iron targets under the high power ion- and electron-beam treatment *Surf. Coat. Technol*. **2012**, *212*, 79–87.
64. Bryukhovetsky, V.V.; Lytvynenko, V.V.; Startsev, O.A.; Myla, D.E.; Volkov, Yu.N.; Rak, O.L. Mechanisms of deformation induced by high-current pulsed electron beam irradiation. *Mater. Lett.* **2024**, *367*, 136642.